To appear in: **Iranian Journal of Earth Sciences (Iran J. Earth. Sci.)**

E-ISSN: 2228-785X Print ISSN: 2008-8779

Received: 31 August 2024 Revised: 17 February 2025

Accepted: 28 February 2025

DOI: https://doi.org/10.57647/j.ijes.2025.16976

Original Research

Geology, Ore-forming Fluid Chemistry, Sr-Nd Isotopes, and Petrogenesis in the Nasim Copper Deposit, NW Bardaskan area, NE Iran

Touran Ramezani Abbakhsh [1], Mohammad Hassan Karimpour[2*], Hossein Azizi [3], Saeed Saadat[4], Yoshihiro Asahara[5], Behnam Rahimi[2]
[1]*Department of Geology, Faculty of Science, Ferdowsi University of Mashhad, Mashhad, Iran*
[2]*Research Center for Ore Deposit of Eastern Iran, Faculty of Science, Ferdowsi University of Mashhad, Mashhad, Iran*
[3]*Department of Mining, Faculty of Engineering, University of Kurdistan, Sanandaj, Iran*
[4]*Department of Geology and Petroleum Engineering, Mashhad Branch, Islamic Azad University, Mashhad, Iran*
[5]Department of Earth and Environmental Sciences, Graduate School of Environmental Studies, Nagoya University, Nagoya 464-8601, Japan
* Corresponding author: karimpur@um.ac.ir

Abstract

The Nasim copper deposit is situated in Bardaskan area, northeast of Iran. The geological units include basalt, andesite, trachyandesite, and sedimentary rocks. Conglomerate composed of volcanic fragments and nummulitic limestone has been deposited as a result of subsequent volcanic activity. The majority of trachyte to andesitic rocks that plot within the shoshonite series and exhibit high LREE/HREE and Th/Yb ratios suggest an active continental margin. Elevated Th and Nb values indicate a minor continental crustal assimilation event. Initial $^{87}Sr/^{86}Sr$ and εNd (i) of the volcanic rocks (t=40 Ma) are 0.7042 to 0.7046 and +4.96 to +5.10 in the Nasim copper deposit, which confirms that it occurred during the continental margin subduction zone .The volcanic rocks were formed in a non-marine environment, and mineralization occurred within the conglomerate bands. The Nasim copper deposit has considered as Manto-type deposit, and chalcocite mineralization occurred after the formation of the conglomerate. The absence of epidote associated with chalcocite suggests low iron content and reducing conditions in the ore-forming fluid of the Nasim deposit. Therefore, the source of mineralization is not magmatic, and further studies on the origin of this deposit should be conducted.

Keywords: *Manto type deposit, Sr-Nd isotope ratios, Copper mineralization, Eocene magmatism, northeast Iran.*

1. Introduction

The term “Manto-type deposits” encompasses a broad spectrum of strata-bound deposits formed in various regions worldwide (Boric et al., 2002; Wilson et al., 2003; Wilson and Zentilli, 2006; Shen et al., 2020). Hydrothermal solutions originate from fractures and precipitate minerals within suitable host rocks, such as conglomerate or pyroclastic formations. The Manto-type strata-bound mineralization is typically confined to a specific horizon characterized by high porosity. In essence, this mineralization exhibits epigenetic characteristics, with structural factors playing a predominant role in its formation (Boric, 2002; Kojima et al., 2003; Pollard, 2006). In Iran, over 30 significant Manto-type copper deposits have been reported from Bardaskan (This study; Ghelichkhani et al., 2021; Ramezani Abbakhsh et al., 2023; Salehpour et al. 2025), Sabzevar (Najmi et al., 2016; Entezari Harsini et al., 2017), Saveh-Jiroft (Karimpour et al. 2021; Mollai et al. 2021; Abdolahadi et al. 2025), Alborz-Azerbaijan (Hassanzadeh et al., 2002; Arjmandzadeh et al. 2020; Nazari et al. 2023; Ousta et al. 2024) and Sanandaj-Sirjan (Boveiri Konari et al., 2013; Dabiri et al. 2018) zones (Fig. 1). The Nasim copper mine is the most significant Manto-type deposit type in the Bardaskan region, situated in the northeastern part of Iran, approximately 50 kilometers northwest of Bardaskan, Khorasan Razavi Province. The mine holds a reserve of approximately 13 million tons and an average grade of copper of 0.6 wt.% (Parsi Con Kavan Company, internal report).

The primary objective of this research study is to present a comprehensive overview of geological, alteration, geochemical, and mineralogical studies conducted in the region. This study serves as a foundation for understanding the intricate relationship between paragenesis, alteration, and ore-forming fluid chemistry. By elucidating these factors, it facilitates the exploration of analogous deposits in other regions of Iran.

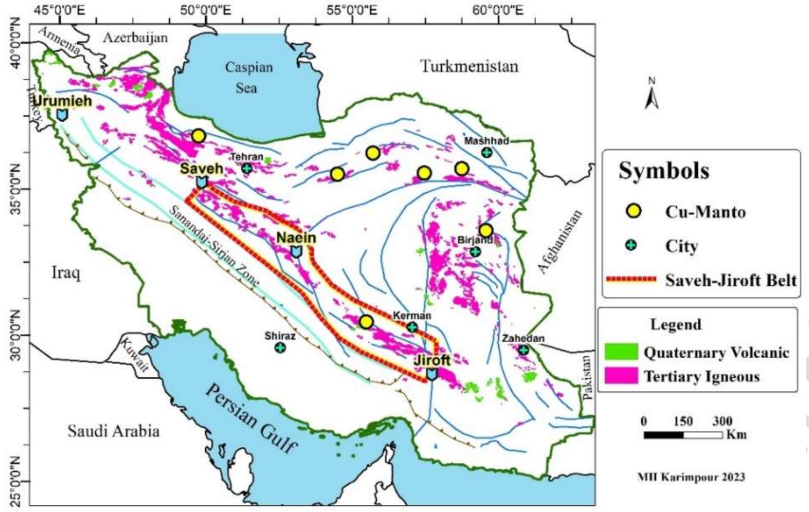

***Figure* 1.** Major geological subdivisions of Iran (Karimpour, 2023) and location of some of the most important Manto-type deposits in Iran. The most important Manto-type deposits in Iran.

2. Geological Background

In this article, we divide the volcanic-plutonic complexes in northeastern Iran into three areas based on different mineralization systems: 1- The Cretaceous volcanic-plutonic rocks North of the Bardaskan area (Fig. 2); 2- The Eocene volcanic rocks northwest of the Bardaskan area (Fig. 2); 3- The Eocene Kashmar-Khaf magmatic belt (Fig. 2), which is located above the Doruneh fault (Fig. 2).

2.1. North of the Bardaskan area (near Oryan)

Magmatism occurred during the Cretaceous period, and was related to the activity of submarine volcanoes (Moghadam et al., 2014) (Fig. 2). These rocks are classified into lower and upper sections based on their age and composition. The lower section is primarily composed of deep marine sediments interspersed with volcanic rocks. The sedimentary rocks in this section include chert, shale, and sandstone, while the volcanic rocks consist of pyroclastic rocks with diverse compositions and rhyolitic, dacite, and andesite lavas. The upper section comprises a series of sandstones interspersed with microconglomerate, globotruncana pelagic limestone, tuff, sandstone, volcanic rocks, limestone, and marl (Moghadam et al., 2014).

The late Cretaceous volcanic-sedimentary sequence in the north of the Bardaskan area contains manganese and massive copper sulfide deposits (Maghfouri et al., 2015) that include Nodeh copper deposit (Nasrollahi et al., 2012), Astaj manganese deposit (Aghdam et al., 2018), Homai manganese deposit (Nasiri et al., 2010), Chashme Sefid manganese deposit (Ghanbari et al., 2009), and Zakiri manganese deposit (Taghizadeh et al., 2012).

2.2. Northwest of the Bardaskan area

In the northwestern region of Bardaskan, volcanic rocks that host copper Manto deposits comprise basalt, andesite, and trachyandesite (Fig. 2). Sedimentary rocks include conglomerate, nummulitic limestone, marl, and evaporite sediments. The Northwest Bardaskan area is bounded to the north by gypsum ferrous red layers, Neogene conglomerate, and Quaternary sediments, while to the south, it is restricted by volcano-pelagic and late Cretaceous ophiolites. In the upper portion of the conglomerate, a nummulitic limestone unit is present. Based on the presence of nummulites, the age of the limestone is estimated to be Eocene (Schaub, 1981; Papazzoni, 1993; Papazzoni and Sirotti, 1995). Age dating in the Zangalou area (north-east of Nasim deposit), using the U-Pb zircon on andesite, gives an age between 41.2 and 38.4 Ma (Bartonian) (Ghelichkhani et al., 2023). Some of the most important Manto-type deposits in the northwest Bardaskan area are Cheshme Marzieh (Soltani and Fardost, 2016), Rizab (Jonidi and Fardost, 2017), Dehne Siah, Kalabri (Jabari et al., 2017), Sharif Abad (Ebrahimi et al., 2018), Taranom (Entezarab, 2018), Kimia (Amini Zahan et al., 2019), Zangalou deposit (Ghelichkhani et al., 2023) and Nasim (Fig. 2).

2.3. Kashmar-Khaf magmatic belt

The Kashmar- Khaf volcanic- plutonic belt is located in northeastern Iran with a length of 216.7 km and NW-SE trend (***Karimpour,*** 2023) (Fig. 2). According to studies by Mazhari et al (2015), Golmohammadi et al (2015), Karimpour et al (2017), and Hosseini et al (2018), the source granitoid pluton is I-type which was developed in a subduction tectonic setting. The age of the source pluton in this belt is Eocene, 39.1 ± 0.6 to 38.3 ± 0.5 Ma (Golmohammadi et al., 2015), based on zircon U–Pb, 40.7-41.7 Ma ages (Karimpour et al., 2017), and with a radiometric age of 39.8 Ma (Hosseini et al., 2018). Mineralization has occurred as skarn-type deposit, Iron oxide, copper- and gold (IOCG), and porphyry deposit in this belt (Karimpour et al., 2017) that includes Sngan skarn deposit (Golmohammadi et al., 2015), Tannurjeh porphyry (Cu-Au) deposit (Hossieni et al., 2018), IOCG deposits such as Kuh-e-Zar Au (Mazloumi Bajestani et al., 2008), Namegh (Au) (Taghadosi and Shafaroudi, 2018), and Bahariyeh (Cu) (Najmi et al., 2023).

There is no copper Manto-type deposit along the Kashmar-Khaf magmatic belt, the most significant mineralization associated with granitoid rocks. However, the volcanic rocks in the Northwest of the Bardaskan area exhibit a comparable age (Fig. 2).

Figure **2. Location of the Kashmar-Khaf magmatic belt and Manto-type deposits in the** northwest of Bardaskan **(modified from Karimpour, 2023).**

3. Material and Methods

3.1. Petrography and Mineralography

Sampling and structural studies were conducted during fieldwork. A total of 140 thin sections and 52 polished sections were examined, and a geological map with a scale of 1:1000 was prepared. Additionally, drilling logs from the 1500-meter section in 30 boreholes were analyzed.

3.2. Major and trace elements geochemistry

Thirteen samples, devoid or exhibiting only minor alterations from volcanic units, were selected for chemical analysis. The selected samples were analyzed in the East Amethyst Lab (Mashhad, Iran) for major oxides by wavelength dispersive X-ray fluorescence (XRF) spectrometry using fused disks and the Philips PW 1410 XRF spectrometer, A set of international and Iranian rock standards including MRG-1, MG-4, JG-2, JR-1, SY-2, SY-3, JSL-1, MK-1, NIM-S, and NCS-307, were used for calibration. After crushing and pulverizing the samples, they were fused using lithium metaborate/tetraborate flux and digested using nitric acid. The resulting disks were placed in the spectrometer, and an X-ray was directed at the sample under conditions close to a vacuum. The elements were identified based on the wavelength and frequency of the X-rays emitted by the atoms in the sample (Table 1).

Furthermore, these samples were forwarded to MSA-LABS (Vancouver, Canada) for analysis of trace elements by inductively coupled plasma mass spectrometry (ICP-MS) (Table 1). Samples were dried and prepared to meet the passing criteria of 85% - 75µm for rock. Lithium borate fusion is a commonly employed sample decomposition technique, particularly for samples that are challenging to dissolve in acids, such as refractories and metal oxides. During this process, weighed samples are heated in a high-temperature muffle furnace at 1000°C in the presence of lithium borate flux. The resulting fused sample is subsequently cooled and dissolved in mineral acids. The resulting solution is subsequently analyzed using Inductively Coupled Plasma-Mass Spectroscopy. ICP-MS standards are assayed by validated ICP and wet chemical procedures to obtain the certified value. The errors in the ICP–MS data, based on the manufacturer’s information were less than 5% and as little as 3%. The equipment model used for ICP-MS analysis is Agilent 7900 ICP-MS.

3.3. Sr-Nd isotope ratios

Sr and Nd isotopic ratios were measured for five samples by using a GVI IsoProbe thermal ionization mass spectrometer (TIMS) at the University of Nagoya, Japan (Table 2). The mass fractionations of the Sr and Nd isotope measurements were corrected according to the following equations: (^{87}Sr/ ^{86}Sr) = 0.1194 and (^{143}Nd/^{144}Nd) = 0.7219, respectively. Azizi and Asahara (2013) describe the quantitative and isotope analyses in detail. Mass fractionations during Sr and Nd isotope measurements were corrected according to the ratios of (^{86}Sr/^{88}Sr) = 0.1194 and (^{143}Nd/^{144}Nd) = 0.7219, respectively. In this work, NIST-SRM987 and JNdi-1 (Tanaka et al., 2000) were used as natural Sr and Nd isotope ratio standards, respectively. During this study, repeated analyses of the NIST-SRM987 and JNdi-1 standards gave mean values of (^{87}Sr/^{86}Sr) = 0.710256 ± 0.000006 (n = 5) and (^{143}Nd/^{144}Nd) = 0.512110 ± 0.000002 (n = 2), respectively.

4. Results

4.1. Field relationship and petrography

The geological units in the area comprise basalt, andesite, trachyandesite, and sedimentary rocks, exhibiting a northeast-to-southwest trend (Fig. 3). The volcanic rock sequence is estimated to have a thickness of approximately 1 to 1.5 kilometers. Notably, within this sequence, no evidence of interlayered sedimentary rocks or pillow lava textures was observed within the basaltic formations. Additionally, several dioritic dykes were identified in the area (Fig. 4 a, b).

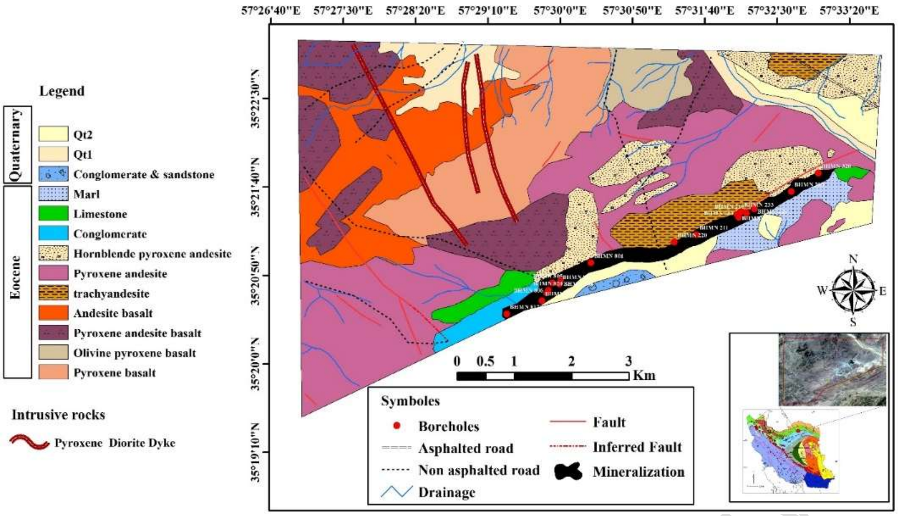

Figure **3.** Geological-mineralization map of the Nasim copper deposit (modified from Ramezani Abbakhsh et al., 2023).

Basalt:

Basaltic rocks are the oldest unit in the study area and are classified as olivine pyroxene basalt, pyroxene basalt, andesite basalt, and pyroxene andesite basalt (Fig. 3). These rocks, with an extension of about 0.5 to 2 km^2, were found in the north, west, and northwestern parts of the study area. The basaltic rocks exhibit porphyritic and amygdaloidal textures. They are composed primarily of plagioclase phenocrysts (10-20%) and pyroxene phenocrysts (3-15%), with 3-5% magnetite in the groundmass. The amygdales are filled with carbonate minerals. The pyroxene grains are commonly augite and the plagioclase are andesine to labradorite (Fig. 5 a).

Andesite:

The outcropping of andesitic rocks is distributed throughout the southwestern, central, and southeastern regions, extending approximately 2 to 5 km^2 (Figures 3 and 4a). This unit is classified into two subunits: pyroxene andesite and hornblende pyroxene andesite. The texture of these rocks is phaneritic, amygdaloidal, and porphyritic. The phenocrysts include 38-40% euhedral plagioclase (andesine), 7-10% clinopyroxene (augite), and 5-7% hornblende. This rock contains 3 to 5% magnetite. The rocks have undergone propylitic alteration, resulting in the formation of secondary minerals such as carbonate and chlorite. The amygdales are carbonate, zeolite, and minor quartz (Fig. 5 b).

Trachyandesite:

Trachyandesite covers an area with an extension of approximately 3 km^2 in the northeast, and about 2.5 km^2 in the southern parts, in contact with the mineralization zone (Fig. 3). It has a porphyritic, and trachytic texture with sanidine and magnetite minerals (3-5 %) in groundmass. Plagioclase (oligoclase to andesine) is the main phenocryst (10-12%) (Fig. 5 c). This unit underwent propylitic alteration, resulting in the filling of the cavities with carbonate, zeolite, and quartz.

Pyroxene diorite porphyry:

Several dykes with diorite composition have cut the surrounding volcanics (Fig. 3 and 4 b). These dykes show a porphyritic texture and contains 45-50% plagioclase (oligoclase) and 12-15% pyroxene (augite) (Fig. 5 d). This unit was affected by propylitic alteration.

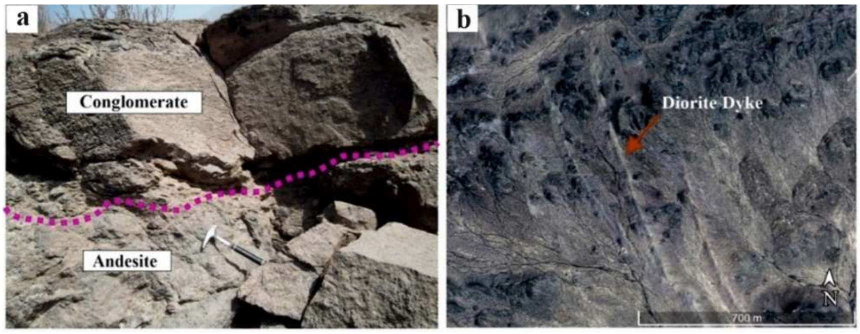

Figure **4.** Field Observation: (a) Contact between conglomerate and andesite. (b) Outcrop of the porphyritic diorite dyke

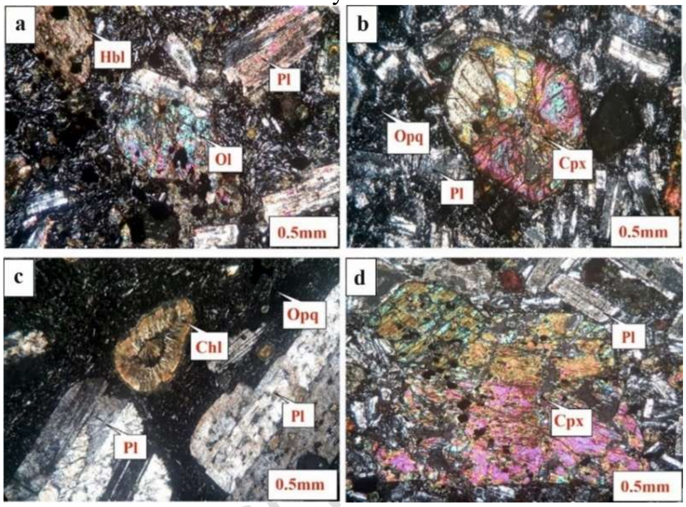

Figure **5.** Photomicrographs of (a) porphyritic texture in olivine pyroxene basalt. (b) andesite with clinopyroxene (augite), plagioclase, and opaque in the groundmass. (c) trachytic texture in trachyandesite and amygdule which was filled by chlorite. (d) Pyroxene diorite porphyry.
Abbreviations; (Pl = Plagioclase, Cpx = Clinopyroxene, Hbl= Hornblende, Ol= olivine, Chl = Chlorite, Opq = Opaque) (Whitney and Evan, 2010).

Conglomerate:

The conglomerate holds significant importance in the study of Cu-Manto mineralization within the northwestern region of the Bardaskan area, as depicted in Figure 3. During the Eocene period, rocks exposed in the region were eroded, carried by water, and deposited as conglomerates. Therefore, this conglomerate contains important information about the characteristics of the rocks in the region during the Eocene period.

This conglomerate, with approximately 25 m thickness, is formed after volcanic activity and erosion processes (Fig. 4a). This unit contains fragments of more than 90 to 95% volcanic rocks and 5 to 10% volcanic rocks (Fig. 6). In the same area, a few fragments of shale were also identified (Fig. 6 a). The size of the fragment changes from 2 to 6 cm and includes andesite, pyroxene andesite, trachyte, andesitic tuff, dacite, diorite, monzonite, monzodiorite, and diorite porphyry (Fig 6 a, b, c). The size and quantity of the fragments diminish as they ascend (Fig. 6 a). The conglomerate cement consists of fine-grained material from eroded volcanic rocks (Fig. 6 a, b, and seven a, b) and magnetite that have originated from eroding volcanic rocks. The volcanic rocks contain 2-3% magnetite. In the upper section of the conglomerate, limestone dominates the cement composition, as evidenced by Figures 6 c and 7 a.

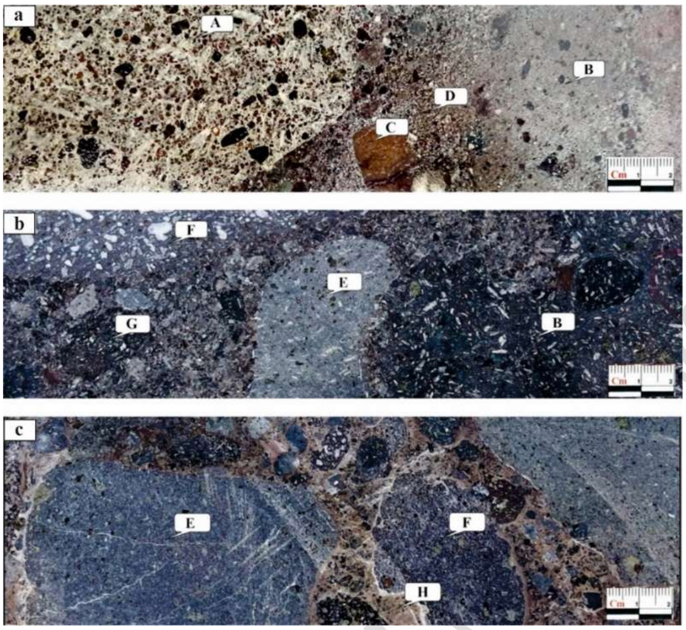

Figure 6. Core sample photographs of conglomerates containing various volcanic and intrusive fragments at the Nasim copper deposit. (a) A conglomerate with volcanic cement (A): Monzonite with propylitic alteration, (B): Andesite with plagioclase in the groundmass, (C): Shale, (D): Volcanic cement. (b) Rounded conglomerate fragments with volcanic cement (B): Andesite with plagioclase in the groundmass, (E): Diorite porphyry with propylitic alteration (epidote), (F): Pyroxene andesite with amygdaloidal texture-filled with silica and carbonate, (G): Andesite with magnetite in the groundmass (mostly magnetite). (c) Conglomerate with carbonate cement (F): Andesite with magnetite in the groundmass (mostly magnetite), (E): Pyroxene andesite with bright and fine-grained groundmass, (H): Carbonate cement (modified from ***Ramezani Abbakhsh et al., 2023).***

Limestone:

The Paleocene-Eocene conglomerate is covered by creamy and gray limestone. The thickness of limestone varies from 5 to 35 m in this area (Fig. 3). This unit is a packstone and wackestone (Fig. 6 c) that contains clastic fragments: 0.5-1% quartz (0.1-1 mm), 0.5-2% plagioclase (1-2 mm), 0.5-3% andesite fragments (0.1- 0.8mm). Some small volcanic clasts are found in the lower part of the limestone at gaining to conglomerate (Fig. 7 a, b). The limestone consists of nummulite fossils (8-12%) (Fig. 7 c).

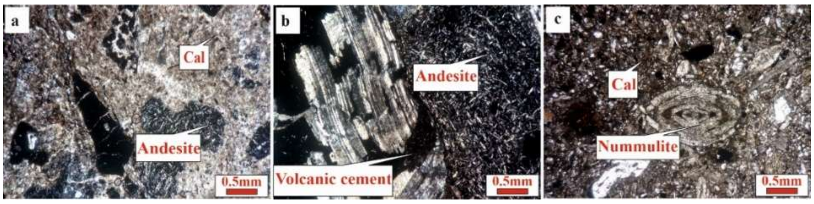

***Figure* 7.** Photomicrographs of conglomerate in the Nasim area: (a) A conglomerate with andesite fragments and carbonate cement. (b) A conglomerate with volcanic cement. (c) Limestone with nummulite fossil. *Abbreviations; (Cal= Calcite*) *(Whitney and Evan, 2010).*

4.2. Mineralization and Alteration

The Cu mineralization in the Nasim deposit primarily occurred within conglomerates, fractures, and faults (Fig. 3). Limited mineralization has also been observed in carbonate rocks with a thickness of 5-35 m within the Nasim copper deposits. The porosity in the conglomerate and the tectonic structure of the region played a significant role in the mineralization (Fig. 8). The mineralization zone exhibits a thickness variation ranging from approximately 1 to 25 m, with an average copper grade of 0.6 wt.%. The mineralized zone's dip is approximately 45 degrees to the southwest (Fig. 3) and is situated within the trachyandesite, with a thickness of approximately 1300 m and an age of 42-38 Ma (Fig. 8).

Chalcocite is the main and primary sulfide mineral which occurs as disseminated, veinlet, and open-space filling and malachite is the most abundant oxidized mineral that fills conglomerate cavities just at the surface (Fig. 9 a, b, c).

Alteration at the Nasim deposit is divided into two stages:

(a) *Stage 1*: The initial stage of the conglomerate's formation predates the conglomerate's formation itself. These alterations include propylitic (epidote and chlorite), zeolite, silicification, and carbonate (Fig. 6 a, b). Subvolcanic (monzonite and diorite, etc.) and volcanic rocks were eroded, and their fragments were transported by water flow, resulting in the formation of the conglomerate in this region. Consequently, these alterations occurred after the formation of volcanic rocks and prior to the formation of the conglomerate and mineralization.

(b) *Stage 2:* This stage was formed after the formation of a conglomerate during the mineralization. This stage comprises only chlorite and calcite alteration (Fig. 9c). Consequently, it was formed simultaneously with mineralization.

Chlorite occurs as veinlet, and open-space filling texture and increases toward the mineralization zone, which shows its association with chalcocite (Fig. 9 c).

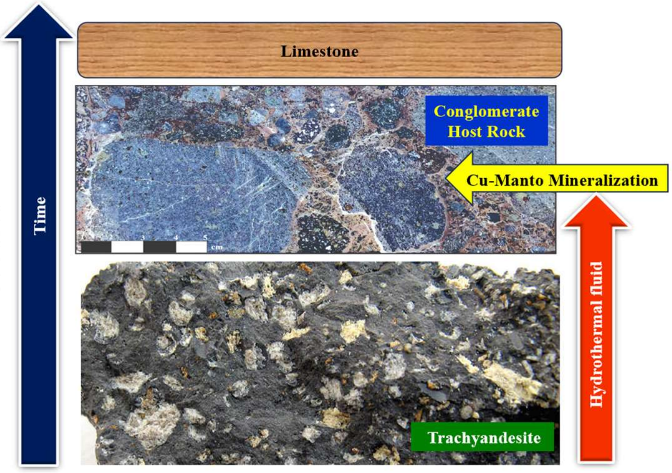

***Figure* 8.** An illustration of the location of mineralization in the conglomerate horizon at the Nasim copper deposit (modified from Karimpour, 2023).

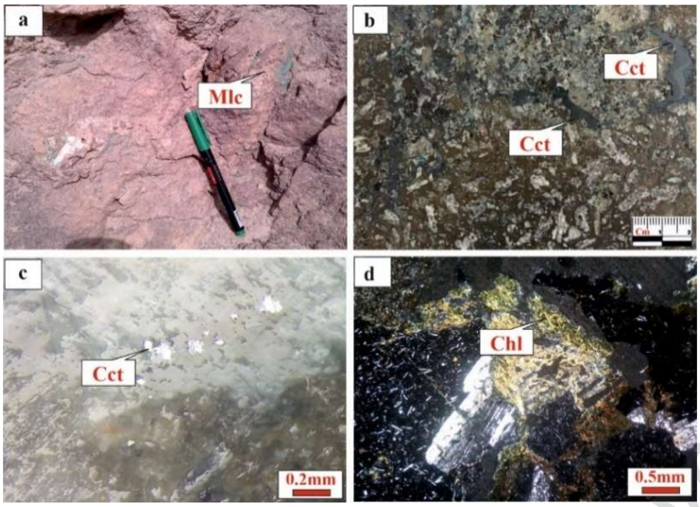

***Figure* 9.** Field, core, and microscopic photographs of mineralization zones in the Nasim deposit: (a) Malachite in the conglomerate (b) Chalcocite veinlet in the core sample (c) Chalcocite veinlet (d) Chlorite in the conglomerate. *Abbreviations; (Cct= chalcocite, Chl=Chlorite, Mlc= Malachite) (Whitney and Evans, 2010).*

5. Discussion

Manto-type mineralization, characterized by its presence in the northwestern Bardaskan region (e.g., Nasim and Zangalu), is exclusively confined to the conglomerate situated above the volcanic formations. Consequently, our focus in this section is the petrogenesis and tectonic setting of the volcanic rocks, followed by an examination of the related ore-forming deposits

5.1. petrogenesis and magma sources

Whole rock chemistry

SiO_2 contents of volcanic rocks vary from 50.51 to 58.10 wt.%, (Table 1). Most of the samples have a low LOI. The TiO_2 contents are low (<1 wt%) and the Al_2O_3 contents vary from 15.50 to 17 wt%. The CaO varieties are from 22.65 to 9.11 wt% and the K_2O varies from 2.02 to 4.55 wt.%. The samples show high Na_2O (2.7 to 6.10 wt%) and K_2O (2.02 to 4.55 wt%) contents. Rb concentrations are less than 120 ppm in most of the samples, while Sr and Th concentrations range from 334.4 to 748.2 ppm, and 2.63 to 4.99 ppm, respectively. Samples are predominantly plotted in the trachy basalt, basaltic trachyandesite, and trachyandesite fields, as well as the sub-alkaline field in the Na_2O-K_2O versus SiO_2 diagram (Le Bas et al., 1986) (Fig. 10). Most samples plot in the Shoshonite series in the K_2O versus SiO_2 diagram (Peccerillo and Taylor, 1976) (Fig. 11).

Table 1. Major (wt.%), trace, and rare earth element (ppm) composition of volcanic rocks in the study area.

S. N	NA-01	NA-15	NA-22	NA-24	NA-32	NA-11	NA-12	NA-13	NA-14	NA-38	NA-18	NA-23
Rock type	1	2	1	2	1	1	1	1	1	1	2	2
SiO_2	53.25	50.51	53.91	52.81	57.31	51.38	54.48	54.06	58.10	56.20	52.10	53.91
TiO_2	0.87	0.71	0.85	0.81	0.90	0.76	0.8	0.81	0.70	0.82	0.82	0.85
Al_2O_3	15.80	14.90	16.46	15.90	16.38	17.01	16.28	16.50	15.50	15.71	15.76	16.46
FeO_t	3.93	5.2	3.57	4.78	2.68	5.25	3.6	5.64	4.58	2.88	3.88	3.57
Fe_2O_3	5.9	7.86	5.36	7.17	4.02	7.88	5.14	8.47	6.87	4.32	5.83	5.36
MnO	0.11	0.17	0.21	0.17	0.12	0.14	0.11	0.11	0.13	0.06	0.13	0.21

MgO	3.44	9.11	5.08	7.28	2.65	4.89	4.13	3.30	3.20	3.16	5.72	5.08
CaO	4.38	6.10	4.87	5.42	5.70	4.70	2.7	3.2	3.40	3.86	4.92	4.87
Na_2O	4.55	2.02	3.03	2.49	3.88	2.25	3.38	2.53	2.72	3.06	3.67	3.03
K_2O	3.57	2.90	3.78	3.50	3.65	4.30	5.07	4.20	4.10	4.03	3.40	3.78
P_2O_5	0.56	0.27	0.35	0.32	0.61	0.36	0.65	0.31	0.33	0.42	0.67	0.33
LOI	2.31	1.5	1.47	0.86	1.65	1.06	2.2	0.98	1.47	1.63	1.90	1.82
Total	100.64	100.65	100.54	100.63	100.36	100.59	100.66	100.69	100.62	100.52	100.61	100.59
V	189	259	271	252	175	300	213	269	242	198	178	322
Cr	38	623	329	405	45	390	32	289	390	56	126	24
Cs	3.26	2.21	2.7	5.7	2	2.9	3.5	3.1	2.8	1.25	4.41	2.9
Ba	318.5	154.3	447.6	264.4	298.7	312.5	312.6	345.8	402.7	228.7	231.5	800.7
Rb	135.6	99	131	114	102.9	119	188.1	115	117	115.2	153.4	110
Sr	442	412.4	621	437.5	640.9	334.4	451.8	399.9	378.8	609.9	527.4	748.2
Y	16.4	16.2	16.7	19.9	20.6	16.1	15.2	15	15.8	14.3	14.2	18.4
Zr	104	98	78.2	83	111	101	114	113	114	103	102	78
Nb	6.8	3.9	4.7	4.9	6	4.8	7.3	6	6.1	5.9	6.7	4
Ga	15.5	13.7	13.5	16	17.3	16.1	17	18	13.9	18.1	15.7	18.7
Sn	<5	<5	<5	<5	<5	<5	<5	<5	<5	<5	<5	<5
Hf	2.5	1.6	1.2	2.4	3.1	1.3	2.7	1.6	1.5	2.7	2.4	2.3
Ta	0.5	0.5	0.3	0.4	0.4	0.1	0.5	0.3	0.3	0.4	0.6	0.2
W	<1	<1	<1	<1	<1	<1	<1	<1	<1	1	<1	<1
Th	4.93	3.9	3.3	3.28	4.68	3.78	5.33	5.1	4.95	4.33	4.99	2.63
U	1.23	1.2	1.4	1.5	1.6	1	1.53	1.2	2.5	3.61	1.65	0.9
La	17.8	13	15.3	16	17.7	13.6	17.5	13.4	15.8	16.4	15.8	12.7
Ce	35.1	32	29	27.1	35.7	32.1	35.3	29	31.2	33.2	31.3	27
Pr	4.33	3.2	3.9	4.3	4.59	3.7	4.46	4.1	3.9	4.28	3.91	3.25
Nd	17.1	17	17.4	18	19.3	17.2	18.2	16.6	17	17.3	16.5	15
Sm	3.41	3.1	3.1	3.5	3.82	3.1	3.6	3.2	3.3	3.4	3.15	3.67
Eu	0.99	0.76	0.79	0.95	1.04	0.71	0.99	0.75	0.72	0.97	0.9	1.29
Gd	3.45	2.79	2.34	3.24	3.57	2.24	3.22	2.12	2.21	3.18	3.13	3.66
Tb	0.48	0.47	0.4	0.57	0.59	0.38	0.48	0.35	0.42	0.45	0.41	0.53
Dy	2.85	2.95	2.61	3.47	3.64	2.52	2.84	2.41	2.73	2.59	2.46	3.46
Ho	0.57	0.65	0.52	0.71	0.74	0.52	0.56	0.56	0.59	0.54	0.54	0.7
Er	1.79	1.81	1.55	2.16	2.12	1.6	1.61	1.59	1.66	1.57	1.69	2.09
Tm	0.25	0.29	0.2	0.35	0.3	0.21	0.24	0.22	0.28	0.22	0.23	0.27
Yb	1.66	1.7	1.49	2.06	2.07	1.4	1.67	1.44	1.72	1.42	1.52	2
Lu	0.23	0.25	0.23	0.33	0.34	0.21	0.25	0.23	0.24	0.23	0.23	0.3
Ratios												
Ce/Yb	21.14	18.82	19.46	13.15	17.24	22.92	21.13	20.13	18.13	23.38	20.59	13.5
Eu/Eu*	0.88	0.79	0.9	0.86	0.86	0.82	0.89	0.88	0.82	0.90	0.88	1.08
$(La/Yb)_N$	7.23	5.16	6.92	5.24	5.76	6.55	7.06	6.27	5.88	7.79	7.01	4.28

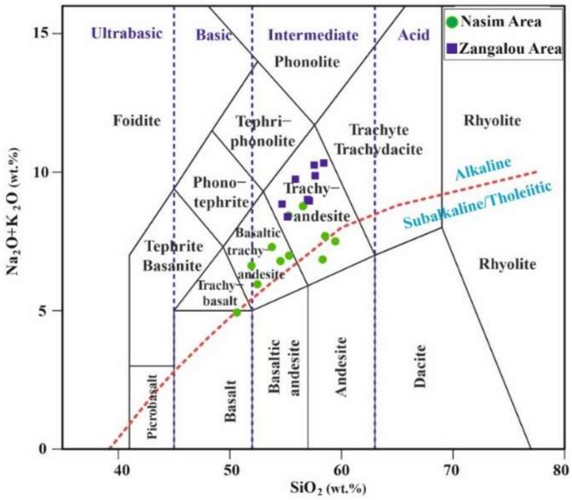

Figure* 10.** Na_2O - K_2O versus SiO_2 diagram (Le Bas et al., 1986), samples from the Nasim area are trachy basalt, basaltic trachy andesite, and trachy andesite and the Zangalou samples are trachyandesite ***(Ghelichkhani et al., 2023).

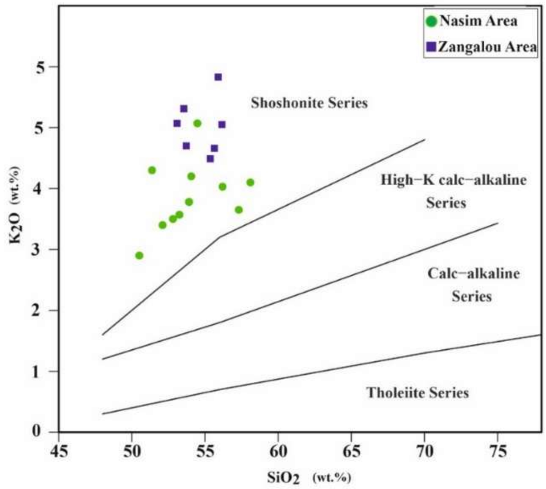

***Figure* 11.** K_2O versus SiO_2 diagram (Peccerillo and Taylor, 1976), all samples from the Nasim area, similar to those from the Zangalou area ***(Ghelichkhani et al., 2023)*,** fall within the Shoshonite series field.

5.2. Tectonic settings

The high Th/Yb ratios of volcanic rocks are plotted in the active continental margin field (Fig. 11). Some higher Th and Nb values suggest possible continental crustal assimilation. These samples are primarily characterized by the depletion of elements such as Nb and Ti while elements like K, Rb, Th, and Sr are enriched (Fig. 12). These characteristics are similar to those observed in subduction zone environments (Green, 1995).

These volcanics exhibit enrichment of Rare-Earth Elements (LREE) compared to Heavy-Fractional Separation Elements (HFSE) in the chondrite normalized trace element spider diagram (Boynton, 1984) (Fig. 13 a). The Eu/Eu* contents of the volcanic rocks in the Nasim area range from 0.86 to 1.09 (Table 1), indicating a weakly negative Eu anomaly (Fig. 13 b). The volcanic rocks exhibit strong enrichment in LILEs (Large Ion Lithophile Elements) such as Cs, Ba, Rb, and K in the primitive mantle-normalized trace element spider diagram (Sun and McDonough, 1989)

(Fig. 13 a). Volcanic rocks were compared with samples from the Zangalu deposit in Figures 10-13. Volcanic samples from the Nasim area include trachybasalt, basaltic trachyandesite, and trachyandesite, while the Zangalu samples consist of trachyandesite (Fig. 10). All samples from the Nasim area are similar to those from the Zangalou area, as both are plotted within the shoshonite series field (Fig. 11). In Fig. 13, the Nasim samples and the Zangalou deposit are plotted in the active margin field, above the mantle field. Similar trends can be observed between the elements of the Nasim and Zangalou regions in both graphs (Ghelichkhani et al., 2023).

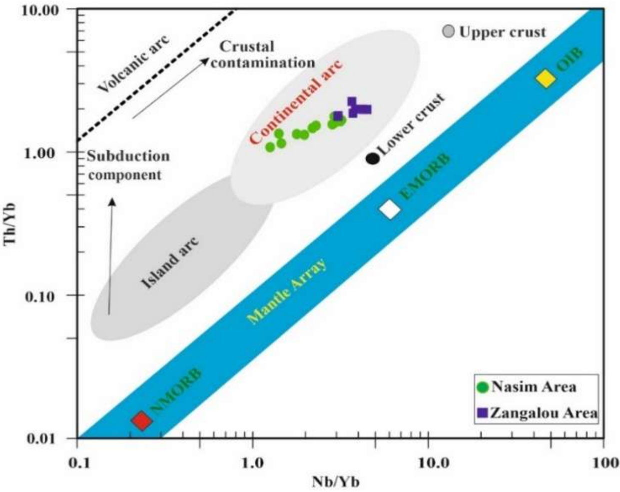

Figure 12. Diagram of Nb/Yb versus Th/Yb (Pearce, 2008). All samples from the Nasim and Zangalou deposit (Ghelichkhani et al., 2023) are plotted in the active margin field above the mantle field. The average values of N-MORB, enriched (E-)MORB, and OIB are taken from Sun and McDonough (1989); the average of the lower and upper crust is taken from Rudnick and Fountain (1995).

,

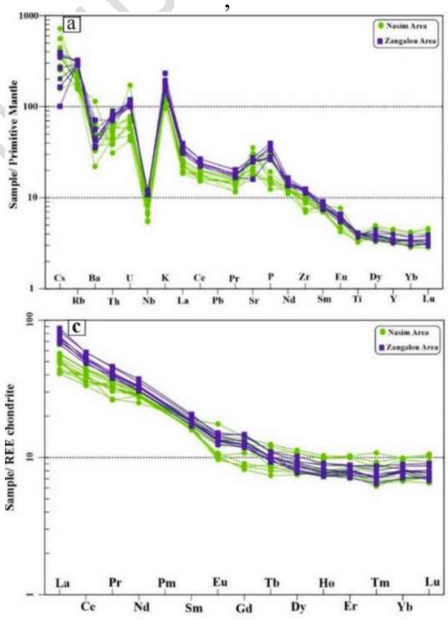

***Figure* 13.** The spiders of the multi-elements diagrams have been normalized to (a) the Primitive Mantle (sun and McDonough, 1989) and (b) the Chondrite-normalized REE diagram (Boynton, 1984) for the volcanic rocks. Similar trends can be observed between the elements of the Nasim and Zangalou regions in two graphs (Ghelichkhani et al., 2023).

5.3. Ore genesis

Sr-Nd Isotope ratios

The εNd$_i$ values and initial ^{87}Sr/^{86}Sr ratios were calculated according to the crystallization age of the volcanic rock units (t = 40 Ma). Initial ^{87}Sr/^{86}Sr and εNd$_i$ of volcanic rocks vary within a limited range of 0**.**7042 to 0**.**7046 and +4.96 to +5.10 (Table 2 a, b). The majority of samples plot within the depleted mantle field in εNd($_i$) vs (^{87}Sr/^{86}Sr)$_i$ diagram and overlap with the IAB (island arc basalt) field (Fig. 14).

Table 2-a. The Rb-Sr isotopic data of five whole-rock samples of volcanic rocks in the study area.

Sample	Rb (ppm)	Sr (ppm)	(^{87}Rb/^{86}Sr)	(^{87}Sr/ ^{86}Sr)$_m$ (2σ)	(^{87}Sr/ ^{86}Sr)$_i$	TDM (Ga)	U-Pb zircon age (Ma)
NA-1	135.6	442	0.9	0.704846 ± 0.000008	0.704342	0.30	40
NA-15	46.0	412	0.3	0.704555 ± 0.000006	0.704372	0.38	40
NA-22	38.2	621	0.2	0.704793 ± 0.000006	0.704692	1.37	40
NA-24	96.3	438	0.6	0.704872 ± 0.000007	0.704511	#VALUE!	40
NA-32	102.9	641	0.5	0.704536 ± 0.000007	0.704272	1.50	40

Table 2-b. The Sm-Nd isotopic data of five whole-rock samples of volcanic rocks in the study area.

Sample	Sm (ppm)	Nd (ppm)	(^{147}Sm/^{144}N)	(^{143}Nd/^{144}Nd)$_m$ (2σ)	(^{143}Nd/^{144}Nd)$_i$	£Nd (i)	TDM (Ga)
NA-1	3.41	17.1	0.1206	0.512879 ± 0.000005	0.512847	5.09	0.30
NA-15	2.51	10.7	0.1419	0.512883 ± 0.000006	0.512846	5.06	0.38
NA-22	2.25	9.1	0.1496	0.512887 ± 0.000006	0.512848	5.10	1.37
NA-32	3.82	19.3	0.1197	0.512872 ± 0.000006	0.512841	4.96	1.50
Sample	Sm (ppm)	Nd (ppm)	(^{147}Sm/^{144}N)	(^{143}Nd/^{144}Nd)$_m$ (2σ)	(^{143}Nd/^{144}Nd)$_i$	£Nd (i)	TDM (Ga)

(^{87}Sr/ ^{86}Sr)i is the initial ratio of (^{87}Sr/ ^{86}Sr) for each sample, calculated using (^{87} Rb/^{86}Sr) and an age of 40 Ma for volcanic rocks ***(Ghelichkhani et al,. 2023). (***^{143}Nd/^{144}Nd) i is the initial ratio of (^{143}Nd/^{144}Nd) for each sample. calculated using (^{147}Sm/^{144}Nd) and (^{143}Nd/^{144}Nd) m and an age of 40 Ma for volcanic rocks ***(Ghelichkhani et al., 2023)***.

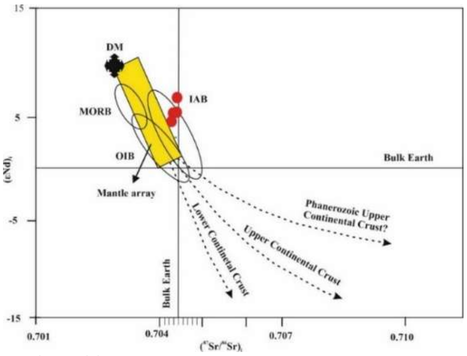

***Figure* 14.** eNd (t = 40 Ma) versus ^{87}Sr/^{86}Sr (i) diagram for Nasim volcanic rocks. The samples extended to a depleted mantle field.

Ore fluid chemistry

Chalcocite is the primary copper mineral in Manto-type copper systems in this area. Conversely, chalcopyrite is the primary mineral in all porphyry copper deposits and massive sulfide deposits globally. Notably, in the Manto-type deposit situated northwest of Bardaskan, chalcocite is not paragenetic with chalcopyrite, pyrite, and magnetite. These minerals are found within conglomerate clasts and exhibit no temporal, spatial, or genetic relationship with chalcocite.

The copper content of chalcocite (Cu_2S) is 79.8%, and it is iron-free, whereas the chalcopyrite ($CuFeS_2$) contains 34.5% copper and 30.5 % iron, and bornite (Cu_5FeS_4) contains a copper content of 63.3% and 11.13% iron. Based on the mineral composition with high copper content and the absence of iron, it can be deduced that the ore-forming fluid chemistry in these systems is characterized by an exceptionally high copper content and a low iron content. Furthermore, the absence of quartz (indicated by chalcocite mineralization) implies that the hydrothermal ore-forming fluid exhibits a deficiency in silica. The chemistry of hydrothermal ore-forming fluid at the time of formation of the Nasim deposit and other Manto copper deposits in the northwest of the Bardaskan area can also be interpreted based on alteration. The absence of epidote ($Ca_2Fe^{3+}{}_{2.25}Al_{0.75}(SiO_4)_3(OH)$) in the syn mineralization (chalcocite (Cu_2S) indicates the low iron content and reducing conditions of the ore-forming fluid in the Nasim deposit.

Several theories have been proposed regarding the origin of Manto-type deposits, with some scientists proposing a volcanic origin (Tosdal and Munizaga, 2003; Wilson and Zentilli, 2006; Liu et al., 2022; Wu et al., 2021).
(a) Igneous rocks that typically contain at least 5% primary magnetite, if they were the source of mineralization, should have hydrothermal solutions rich in iron. However, in the study area, there is no evidence of ferrous minerals such as chalcopyrite or pyrite.
(b) The volcanic rocks in the Nasim copper deposit have not undergone any alteration.
Therefore, based on the ore mineral paragenesis and the chemistry of the ore-forming solution, volcanic rocks cannot be the source of Manto copper deposits in the study area.
Some authors have suggested that intrusive bodies are the source of these deposits (Palacios, 1986; Oliveros et al. 2008).
(a) Conversely, if the source was deep and intrusive, the magmatic fluid would undoubtedly be enriched in silica, iron, and aluminum (Karimpour et al., 2017).
(b) This stands in contrast to the ore-forming fluid chemistry and the mineral paragenesis observed in the Nasim copper deposit. In this deposit, silica and iron-bearing minerals such as chalcopyrite and pyrite are absent from chalcocite, suggesting a non-magmatic origin.
However, the hydrothermal fluid that was transferred through large-scale faults and Cu-mineralization was formed within the conglomerate, which possessed useful porosity. Further research is necessary to determine the origin of this type of deposit. Other factors, such as copper isotope studies in chalcocite and helium elements, must also be considered.
Based on the studies conducted on the paragenesis and solution chemistry of Manto-type deposits worldwide, these deposits can be categorized into two distinct types.
Type 1. Chalcocite: The ore-forming fluid from the first group has been specified to be silica- and iron-free, and its origin is not magmatic. Chalcocite is the most significant primary mineral in these Manto-type systems at Cheshme Gaz (Mahvashi and Malekzadeh Shafaroudi, 2016), Cheshme Marzieh (Soltani and Fardost, 2016), Kalabri (Jabari et al., 2017), Rizab (Jonidi and Fardost,

2017), Taranom (Entezarab, 2018), Sharif Abad (Ebrahimi et al., 2018), Kimia (Amini Zahan et al., 2019), Dehne Siah, Zangalou (Ghelichkhani et al., 2023)**,** and Nasim Copper Mine.

Type 2. Chalcopyrite-Pyrite-Chalcocite groups: In this type of ore, the ore-forming fluid originates magmatically and is characterized by its high iron, silica, and aluminum content (Boric et al., 2002; Wilson et al., 2003; Wilson and Zentilli, 2006; Shen et al., 2020)

The primary distinctions between copper Manto-type deposits in the Nasim and IOCG deposits lie in the concentrations of silica, iron, copper, and the oxidizing and reducing conditions of ore formation (Table 3). Copper deposits associated with iron oxides (IOCG) are silica and iron-rich (chalcopyrite-epidote) and highly oxidized (specularite-epidote).

Table 3. Comparison of paragenesis and geochemical characteristics of the Nasim copper deposit and iron oxide copper type deposit (Ramezani Abbakhsh et al., 2023).

	Copper-Mnto Type (Ghelichkhani et al., 2023; Amini Zahan et al., 2020; Ebrahimi et al., 2018)	**IOCG Type (Karimpour *et al.,* 2021; Najmi *et al., 2023).***
Paragenesis	Chalcocite ±Bornite	Chalcopyrite ± Bornite, specularity, magnetite, pyrite
Ore	Cu	Cu, Au, Ag. REE, U ± Pb-Zn
Alteration	Minor chlorite & calcite (source limestone)	Epidote, chlorite, albite, silicification ± potassic
Geochemistry	Si-Pour, Fe-Pour, reducing, Rich Cu	Si-rich, Fe-rich, highly oxidized
Genesis	Unknown, host rocks: volcano-sedimentary sequences	I-type granitoid
Style of mineralization	Stratabound, porosity control (volcanic conglomerate, pyroclastic)	Vein type, skarn & other types

Depth of Magma generation and oxidation state

Based on the (La/Yb)N ratio, the relative depth of magma generation can be determined (Fig. 14a). The partition coefficient of La in garnet is 0.001, indicating incompatibility of La with garnet (Li et al., 2016; Karimpour and Sadeghi, 2019; Dagva Ochira et al., 2020; Alizadeh et al., 2023). Conversely, the partition coefficient of Yb in garnet is approximately 11, suggesting compatibility of Yb with garnet. At depths exceeding 80 km, the oceanic slab transforms into eclogite. In a subducted slab at depths exceeding 80 km, the (La/Yb)N ratio is interpreted to be greater than 20, which is attributed to partial melting of the eclogitic crust. The (La/Yb)N ratio within the basalt and andesite of the study area is lower than 7 (Fig. 15 a). Consequently, magma formation occurred at a shallow depth within the subduction zone (Fig. 14a). The oxidation and reduction state of magma generation can be determined by examining the Fe+2 and Fe+3 states. Under oxidation conditions, most Fe will be present as Fe^{+3}. Conversely, if magma is oxidizing, magnetite will crystallize. Under reduction conditions, Fe will be in the Fe^{+2} state and substituted into silicate minerals (Ballard et al., 2002; Burnham and Berry, 2012; Trail et al., 2012; Smythe and Brenan, 2016). By measuring the magnetic susceptibility of the rocks, the oxidation and reduction state of magma generation and crystallization can be determined. If the magnetic susceptibility of rock is more than 100×10^{-5} SI it contains magnetite, therefore the magma was generated under oxidation conditions (Abalos and Aranguren, 1998). The magnetic susceptibility of volcanic rock within the study area is between 500 to 1500×10^{-5} SI the magma was generated under oxidation (Fig. 13 b). Based on the ratio of (Eu/Eu)* the oxidation and reduction of magma can be determined. The ratio (Eu/Eu)* of volcanic rocks within the study area is between 0.8-1.2 (Fig. 15 b), therefore the magma was generated under oxidizing conditions. Arc magmas are confirmed to be more oxidized on average than MORB (Jeremy, 2015).

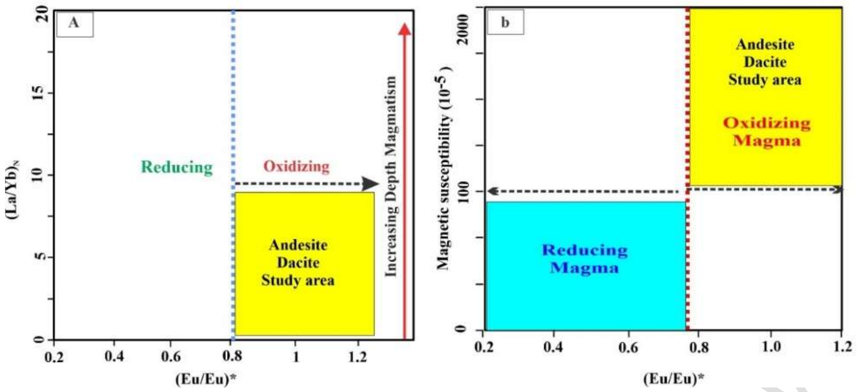

***Figure* 15.** (a) Diagram of (La/Yb)$_N$ versus (Eu/Eu) *. (b) Diagram of Magmatic susceptibility (10^{-5}) versus (Eu/Eu) *.

6. Conclusions

The Nasim copper deposit is one of the most important Cu deposits in the Bardaskan area, northeast of Iran. The primary geological units comprise basalt, andesite, trachyandesite, conglomerate, and nummulitic limestone. The isotope geochemistry (^{86}Sr/^{87}Sr)$_i$ and εNd demonstrate that the volcanic rocks have been derived from enriched lithospheric mantle sources above subduction zone. The primary copper mineral is chalcocite, while quartz is a secondary mineral generated within the host conglomerate. Chalcocite is commonly found in association without quartz within these rocks. This implies that the silica content in the ore-forming fluid is negligible, while the ore-forming fluid in these systems is exceptionally rich in copper and deficient in iron. Additionally, the absence of epidote in the chalcocite-bearing ore zone further confirms the iron-poor nature of the ore-forming fluid and the reducing conditions. If the andesite and trachyandesite were the sources of hydrothermal fluid, they would have to produce an iron-rich solution, as they contain at least 5% primary magnetite. However, there is no evidence of iron-rich minerals such as chalcopyrite and pyrite in the vicinity. Consequently, volcanic rock cannot be the source of propylitic alteration. Finally, we conclude that the Nasim copper deposit and all other deposits in the northwestern Bardaskan region are part of the Manto copper deposits. These deposits lack aluminum and silica in the ore-forming fluid and have a non-magmatic origin. Consequently, only chalcocite is formed. Finally, we recommend conducting isotope studies of copper in chalcocite and helium element analyses to ascertain the origin of the Nasim copper mineralization.

References

Abalos B., Aranguren A. (1998) Anisotropy of magnetic susceptibility of eclogites: Mineralogical origin and correlation with the tectonic fabric (Cabo Ortegal, Spain). Geodinamica Acta 11(6): 271-283. DOI: https://doi.org/10.1016/S0985-3111(99)80017-5

Abdolahadi A., Sheikhzakariaee S.J., Yazdi A., Mousavi S.Z. (2025) Plio-Quaternary Adakite Genesis and Post-collisional Processes: Whole Rock Constraints and Sr, Nd Isotopic Compositions in Alborz Magmatic Belt, Ardabil, Iran. *Journal of Mining and Environmen*t 16(2):737-765. DOI: https://doi.org/10.22044/jme.2024.14781.2801

Aghdam S.S., Ebrahimi Nasrabadi K., Heydarian Shahri M. (2018) Manganese Mineralization of Astaj, an example of volcanic-sedimentary type mineralization in the southwest of Sabzevar. *Iranian Journal of Crystallography and Mineralogy* 25 (2): 411-426 (in Persian).

Alizadeh E., Li H., Babazadeh S., Ma C., Forster M.W. (2023) Late Eocene slab retreat, extension, and mantle upwelling inferred from mantle signatures in potassium-rich magmatism in NE Iran. *International Geology Review* 65(9): 1586–1600. DOI: https://doi.org/10.1080/00206814.2023.2185823

Amini Zahan H., Malekzadeh Shafaroudi A., Karimpour M.H. (2019) Mineralogy and study of fluids involved in Manto Kimia type, north-west of Bardskan, Razavi Khorasan Province. *12th National Conference of Economic Geology Association* (in Persian).

Arjmandzadeh R., Teshnizi E.S., Ahmadi A.A., Mahdavi A., Tavsoli S., Dabiri R. (2020) The mineralogy, geochemistry and genesis of Aghol-Messi sedimentary copper - uranium deposit, Tabas block, Central Iran. *Researches in Earth Sciences* 11(4):47-70. DOI: https://doi.org/10.52547/esrj.11.4.47

Azizi H., Asahara Y. (2013) Juvenile granite in the Sanandaj–Sirjan Zone, NW Iran: Late Jurassic–Early Cretaceous arc–continent collision. *International Geology Review* 55: 1523-1540. DOI: https://doi.org/10.1080/00206814.2013.782959

Ballard JR., Palin MJ., Campbell I.H. (2002) Relative oxidation states of magmas inferred from Ce (IV)/Ce (III) in zircon: application to porphyry copper deposits of northern Chile, *Contrib. Mineral, Petrol* 144 (3): 347–364. DOI: https://doi.org/ 10.1007/s00410-002-0402-5

Boric R., Holmgren C., Wilson NSF., Zentilli M. (2002) The geology of the El Soldado Manto type Cu (Ag) deposit, central Chile. In: Porter, T. M. (Ed), Hydrothermal Iron Oxide Copper–Gold and Related Deposits. *PGC Publishing, Adelaide, Australia*, *A Global Perspective* 2: 185-205.

Boveiri Konari M., Rstad E., Kojima S., Rashidnejad Omran N. (2013) Volcanic redbed-type copper mineralization in the Lower Cretaceous volcano-sedimentary sequence of the Keshtmahaki deposit, southern Sanandaj-Sirjan Zone, Iran. *Neues Jahrbuch für Mineralogie Abhandlungen* 190(2): 107–121. *DOI:* https://doi.org/10.1127/0077-7757/2013/0236

Boynton W.V. (1984) Geochemistry of the rare earth elements: Meteorite studies. In: Henderson P. Ed. Rare earth element geochemistry, Elsevier, New York. *Science Research* 63-114. *DOI:* http://dx.doi.org/10.1016/B978-0-444-42148-7.50008-3

Burnham A.D., Berry A.J. (2012) An experimental study of trace element partitioning between zircon and melt as a function of oxygen fugacity. *Geochim, Cosmochim Acta* 95: 196–212. *DOI:* https://doi.org/10.1016/j.gca.2012.07.034

Dabiri, R., Akbari-Mogaddam, M., Ghaffari, M. (2018) Geochemical evolution and petrogenesis of the Eocene Kashmar granitoid rocks, NE Iran: Implications for fractional crystallization and crustal contamination processes. *Iranian Journal of Earth Sciences* 10(1):68-77.

Dagva Ochira L., Oyunchimeg T.U., Enkhdalai B., Safonova I., Li. H., Otgonbaatar D., Soh Tamehea L., Sharav D. (2020) Middle Paleozoic intermediate-mafic rocks of the Tsoroidog Uul' accretionary complex, Central Mongolia: Petrogenesis and tectonic implications. *Lithos* 376–377: 105795. *DOI:* https://doi.org/10.1016/j.lithos.2020.105795.

Ebrahimi S., Arab Amiri A.R., Ghanbari H. (2018) Mineralogical Studies, Alteration, Fluid Intermediates and Stable Isotopes of Sharif Abad Copper Deposit, Bardeskan, North-East of Iran. *Earth Science Quarterly* 30 (117): 135-146 (in Persian).

Entezarab A. (2018) Geology, Mineralogy, Geochemistry and Geophysical Data Interpretation of Ternam Copper Mine, North-West of Bardaskan. *M.Sc, Thesis, Ferdowsi University of Mashhad, Mashhad, Iran.* 171 p (in Persian).

Entezari Harsini A., Mazaheri A., Saadat S., Santos J.F. (2017) Geochemistry, petrology, and mineralization in volcanic rocks located in south Neyshabour, NE Iran. *Journal of Mining and Environment* 8 (2):139-154. *DOI:* https://doi.org/10.1515/geochr-2015-0061

Ghanbari T.M, Moghadasi S (2009) Geology of the Cheshmeh Sefid manganese deposit, Razavi Khorasan province. *The 4th National Geological Conference of Payam Noor University* (in Persian).

Ghelichkhani M., Malekzadeh Shafaroudi A., Karimpour M.H., Homam S.M. (2021) Petrography, geochemistry and tectonic setting of NW Bardaskan volcanic rocks: a case study of Zangalou mine. *Petrological Journal* 12(2): 1-22 (in Persian).

Ghelichkhani M., Malekzadeh Shafaroudi A., Karimpour M.H., Homam S.M. (2023) Zangalou Manto-type deposit in the Sabzevar zone, northeast Iran: Evidence of mineralogy, geochemistry, U–Pb dating, fluid inclusion, and stable isotopes. *Geological Journal* 58(1): 465-496. *DOI:* https://doi.org/10.1002/gj.4607

Golmohammadi A., Karimpour M.H., Malekzadeh Shafaroudi A., Mazaheri S.A. (2015) Mineralogy, geochemistry, and syn-mineralization intrusions age of Sangan mine: an example of giant Ca-Mg-K-rich iron skarn, Khaf, northeast of Iran. *Ore Geology Reviews* 65: 545-563. *DOI:* http://dx.doi.org/10.1016/j.oregeorev.2014.07.005

Green T.H. (1995) Significance of Nb/Ta as an indicator of geochemical processes in the crust-mantle system. *Chemical Geology* 120: 347–359. *DOI:* https://doi.org/10.1016/0009-2541(94)00145-X

Hassanzadeh J., Ghazi A.M., Axen G., Guest B. (2002) Oligomiocene mafic-alkaline magmatism north and northwest of Iran: evidence for the separation of the Alborz from the Urumieh–Dokhtar magmatic arc. *In Geological Society of America Abstracts with Programs* 34 6): 331.

Herazo A., Reich M., Barra F., Morata D., Real I., Pagès A. (2020) Assessing the role of bitumen in the formation of strata bound Cu-(Ag) deposit- its: Insights from the Lorena deposit, Las Luce's district, northern Chile. Ore Geology Reviews 124: 103639. *DOI:* https://doi.org/10.1016/j.oregeorev.2020.103639

Hosseini R., Karimpour M.H., Malekzadeh Shafaroudi A. (2018) Petrography, geochemistry, U-Pb dating, and Sr-Nd isotopes of igneous rocks in Tannurjeh porphyry Au-Cu prospect area NE of Kashmar. *Journal of Petrology* 33: 45-70 (In Persian).

Jabari E., Malekzadeh Shafaroudi A., Karimpour M.H. (2017) Kalabri strata-bound (M anto-type) copper deposit in Eocene volcanic-sedimentary complex of NW Bardeskan, NE Iran. *Advanced Applied Geology* 7(1): 1–19. DOI: HTTPS://DOI.ORG/10.22055/AAG.2017.13066

Jeremy P.R. (2015) The oxidation state, and sulfur and Cu contents of arc magmas: implications for metallogeny. *Lithose* 233: 27-45. DOI: https://doi.org/10.1016/j.lithos.2014.12.011

Jonidi A., Fardost F. (2017) Mineralogy, geochemistry, and genesis pattern of Rizab copper deposit, northwest of Bardeskan, Razavi Khorasan province. *M. Sc, Thesis, Shahrood University of Technology, Shahrood, Iran.*

Karimpour M.H. (2023) Geochemistry, Genesis and Important Features of Cu-Manto Types Deposits and IOCG Type Deposits. *15th ISEG Symposium and Geological Survey, University of Damghan.*

Karimpour M.H., Malekzadeh Shafaroudi A., Mazloumi Bajestani A.R., Schader R.K., Stern C., Farmer L., Sadeghi M. (2017) Geochemistry, geochronology, isotope and fluid inclusion studies of the Kuh-e-Zar deposit, Khaf-Kashmar-Bardaskan magmatic belt, NE Iran: Evidence of gold-rich iron oxide–copper–gold deposit. *Journal of Geochemical Exploration* 183: 58–78. DOI: https://doi.org/10.1016/j.gexplo.2017.10.001

Karimpour M.H., Rezaei M., Zarasvandi A., Malekzadeh Shafaroudi A. (2021) Saveh-Nain-Jiroft Magmatic Belt replaces Urumieh-Dokhtar Magmatic Belt: Investigation of genetic relationship between porphyry copper deposits and adakitic and non-adakitic granitoids. *Journal of Economic Geology 13* (3): 465-506 (in Persian).

Karimpour M.H., Sadeghi M. (2019) A new hypothesis on parameters controlling the formation and size of porphyry copper deposits: Implications on the thermal gradient of the subducted oceanic slab, depth of dehydration and partial melting along the Kerman copper belt in Iran. *Ore Geology Reviews* 104: 522-539. DOI: https://doi.org/10.1016/j.oregeorev.2018.11.022

Kojima S., Astudillo J., Rojo J., Trista D., Hayashi K. (2003) Ore mineralogy, fluid inclusion and stable isotopic characteristics of stratiform copper deposits in the coastal Cordillera of northern Chile. *Mineralium Deposita* 38: 208–216. DOI: https://doi.org/10.1007/s00126-002-0304-5

Kojima S., Trista D., Guilera A., Hayashi K. (2009) Genetic Aspects of the Manto-type Copper Deposits Based on Geochemical Studies of North Chilean Deposits. Resource Geology 59 (1): 87 – 98. DOI: https://doi: 10.1111/j.1751-3928.2008.00081.x

Le Bas M.L., Maitre R.L., Streckeisen A., Zanettin B. (1986) IUGS Subcommission on the Systematics of Igneous Rocks, A chemical classification of volcanic rocks based on the total alkali-silica diagram. *Journal of Petrology* 27(3): 745-750. DOI: https://doi.org/10.1093/petrology/27.3.745

Li H., Xi X.S., Sun H.S., Kong H., Wu Q.H., Wu C.M., Gabo-Ratio J.A.S. (2016) Geochemistry of the Batang Group in the Zhaokalong area, Yushu, Qinghai: Implications for the Late Triassic tectonism in the northern Sanjiang region, China. *Acta Geologica Sinica (English Edition)* 90: 704–721. DOI: https://doi.org/10.1111/1755-6724.12699

Liu B., Kong H., Wu Q.H., Chen S.F., Li H., Xi X.S., Wu J.H., Jiang H. (2022) Origin and evolution of W mineralization in the Tongshanling Cu–polymetallic ore field, South China: Constraints from scheelite microstructure, geochemistry, and Nd–O isotope evidence. *Ore Geology Reviews* 143:104764. DOI: https://doi.org/10.1016/j.oregeorev.2022.104764

Maghfouri S., Hosseinzadeh M.R., Moayyed M., Movahednia M., Choulet F. (2017) Geology, mineralization, and sulfur isotopes geochemistry of the Mari Cu (Ag) Manto-type deposit, northern Zanjan, Iran. *Ore Geology Reviews* 81(1): 10–22. DOI: https://doi.org/10.1016/j.oregeorev.2016.10.025

Maghfouri S., Rastad E., Mousivand F. (2015) Stratigraphic position, origin and characteristics of manganese mineralization horizons in the Late Cretaceous volcano-sedimentary sequence, south-southwest of Sabzevar. *Developments in Economic Geology* 6 (2) (in Persian).

Mahvashi M, Malekzadeh Shafaroudi AM (2016) Cheshmeh Gaz (Nasim) copper deposit, NW Bardaskan: mineralogy, alteration, geochemistry, and determination of model. *Iranian Journal of Crystallography and Mineralogy* 3(24): 419-434 (in Persian).

Mazhari N., Malekzadeh Shafaroudi A., Ghaderi M. (2015) Geology, mineralogy, and geochemistry of Ferezneh ferromanganese anomaly, east of Sangan mines complex, NE Iran. *Journal of Economic Geology* 7(1): 2008-7306 (in Persian).

Mazloumi Bajestani A.R., Karimpour M.H., Rassa I., Rahimi B., Vosoughi Abedini M. (2008) Kuh-E-Zar Gold Deposit in Torbat-e-Heydaryeh, New model of gold mineralization. *Iranian Journal of Crystallography and Mineralogy* 16(3): 363-376 (in Persian).

Moghadam S.H., Corfu F., Chiaradia M., Stern R.J., Ghorbani G. (2014) Sabzevar Ophiolite, NE Iran: progress from embryonic oceanic lithosphere into magmatic arc constrained by new isotopic and geochemical data. *Lithos* 210–211: 224–241.

Mollai H., Dabiri R., Torshizian H.A., Pe-Piper G., Wang W.E. (2021) Upper Neoproterozoic garnet-bearing granites in the Zeber-Kuh region from east central Iran micro plate: Implications for the magmatic evolution in the northern margin of Gondwanaland. *Geologica Carpathica* 72 (6): 461-81. DOI: http://dx.doi.org/10.31577/GeolCarp.72.6.2

Munizaga F., Reyes J.C., Nyström J.O. (1994) Razones isotópicas de los sulfuros del distrito minero de Cerro Negro: Un posible indicador de los depósitos estratoligados de Cu hospedados en rocas sedimentarias lacustres. *Revista Geol, Chile* 21: 189 –195.

Najmi F., Malekzadeh Shafaroudi A., Karimpour M.H., Simon R.P. (2023) The Bahariyeh iron oxide copper–gold deposit, Khaf-Khashmar-Bardaskan magmatic belt, NE Iran: Constraints from geochemical, fluid inclusions, and O-S isotope studies. *Ore Geology Reviews* 159: 105501. DOI: https://doi.org/10.1016/j.oregeorev.2023.105501

Najmi F., Mazhaheri A., Saadat S., Entezari Harsini A. (2016) Review of geology and geochemical exploration in Golcheshmeh Copper deposit, south of Neyshabour (NE of IRAN). *Indian Journal of Fundamental and Applied Sciences* 6 (1):194-205.

Nasiri F., Lotfi M., Jafari M. (2010) Mineralogical studies on the Homaei manganese deposit in the southwest of Sabzevar. *30P th PSymposium on Geosciences, Geological Survey of Iran, Tehran, Iran* (in Persian).

Nasrollahi S., Mousivand F., Ghasemi H. (2012) Nudeh Mn deposit in the upper Cretaceous volcano-sedimentary sequence, Sabzevar subzone. *31P th Symposium on Geosciences, Geological Survey of Iran, Tehran, Iran* (in Persian).

Nazari M., Arian M.A., Solgi A., Zareisahamieh R., Yazdi A. (2023) Geochemistry and tectonomagmatic environment of Eocene volcanic rocks in the Southeastern region of Abhar, NW Iran. *Iranian Journal of Earth Sciences* 15(4): 228-247. DOI: https://doi.org/10.30495/ijes.2023.1956689.1746

Oliveros V., Feraud G., Aguirre L., Ramírez L.E., Fornari M., Palacios C., Parada M. (2008) Detailed 40 Ar/39 Ar dating of geologic events associated with the Mantos Blancos copper deposit, northern Chile. *Mineralium Deposita* 43(3): 281-293. DOI: https://doi.org/10.1007/s00126-007-0146-2

Ousta S.h., Ashja-Ardalan A., Yazdi A., Dabiri R., Arian M.A. (2024) Petrogenesis and tectonic implications of Miocene dikes in the southeast of Bam (SE Iran): Constraints on the development of active continental margin. *Geopersia* 14 (1): 89-111. DOI: https://doi.org/10.22059/geope.2023.364334.648729

Palacios C. (1986) Subvolcanic copper deposits in the coastal range of northern Chile. *Zentralblatt für Geologie und Paläontologie. Teil I, H.9/10, stuttgart,* 1605-1615. DOI: https://doi.org/10.1127/zbl_geol_pal_1/1985/1986/1605

Papazzoni C.A., Sirotti A. (1995) Nummulite biostratigraphy at the Middle/Upper Eocene boundary in the northern Mediterranean area. *Rivista Italiana di Paleontologia Stratigrafia* 101 (1): 63–80. DOI: https://doi.org/ 10.13130/2039-4942/8566

Papazzoni CA (1993) Macroforaminiferi di piattaforma del margine settentrionale della Tetide al limite Eocene medio-Eocene superior. *Ph. D. Thesis,* 240 P. DOI: https://doi.org/ 10.13140/RG.2.1.3727.5049

Pearce J.A. (2008) Geochemical fingerprinting of oceanic basalts with applications to ophiolite classification and the search for Archean oceanic crust. *Lithos* 100: 14–48. DOI: https://doi.org/10.1016/j.lithos.2007.06.016

Peccerillo A., Taylor S.R. (1976) Geochemistry of Eocene calc-alkaline volcanic rocks from the Kastamonu area, northern Turkey. *Contributions to mineralogy and petrology* 58: 63-81. DOI: https://doi.org/10.1007/BF00384745

Pollard P.J. (2006) An intrusion-related origin for Cu–Au mineralization in iron oxide–copper–gold (IOCG) provinces. *Minerlium Deposita* 41 (2): 179–187. DOI: https://doi.org/10.1007/s00126-006-0054-x

Ramezani Abbakhsh T., Karimpour M.H., Azizi H., Rahimi B., Saadat S. (2023) Metallogeny of Manto-copper deposits, special view in Nasim copper deposit, northwest of Bardaskan, Khorasan Razavi, *Journal of Economic Geology* 15(1): 143-174 (in Persian).

Rudnick R.L., Fountain D.M. (1995) Nature and composition of the continental crust: a lower crustal perspective. *Reviews of Geophysics* 33(3): 267-309. DOI: https://doi.org/10.1029/95RG01302

Salehpour S., Arian M.A., Rad A.J., Zarei Sahamieh R., Yazdi A. (2025) Geochemistry and technomagmatic environment of Eocene volcanic rocks in Yuzbashi Chay region, west of Qazvin (Iran). *Iranian Journal of Earth Sciences* 17(1): 1-13. DOI: https://doi.org/10.57647/j.ijes.2025.1701.04

Saric N., Kreft C., Huete C., (2003) Geología del yacimiento Lo Aguirre, Chile. *Revista Geol. Chile* 30: 317 –331. DOI: http://dx.doi.org/10.4067/S0716-02082003000200010.

Schaub H. (1981) Nummulites et Assilines de la Téthys Paléogéne. Taxinotnie, phylogénèse et biostratigraphie. Schweizerische paläontologische Abhandlungen 104-106: 1-238.

Shen P., Pan H., Li Z., Sun J., Shen Y., Li C., Feng H., Cao C. (2020) A Manto-type Cu deposit in the Central Asian Orogenic Belt: The Hongguleleng example (Xinjiang, China). *Ore Geology Reviews* 124 (103656)

Smythe D.J., Brenan J.M. (2016) Magmatic oxygen fugacity estimated using zircon–melt partitioning of cerium. *Earth Planet, Sci, Lett,* 453: 260–266. DOI: https://doi.org/ 10.1016/j.epsl.2016.08.013

Soltani A., Fardost F. (2016) Mineralogy, geochemistry, and genesis of Abri copper deposit, Dari and Cheshme Marzieh, northwest of Doruneh (Doctoral dissertation. *M. Sc, Thesis, Shahrood University of Technology, Shahrood, Iran* (in Persian).

Sun S., McDonough W.F. (1989) Chemical and isotopic systematics of oceanic basalts: implications for mantle composition and processes. *Geological Society, London, Special Publications* 42(1): 313-345. DOI: https://doi.org/10.1144/GSL.SP.1989.042.01.19

Taghadosi H., Malekzadeh Shafaroudi A. (2018) Evidence of probable Cu-Au mineralization in Namagh area, Northeast of Kashamr: Alteration, mineralization, geochemistry and fluid inclusion studies. *Scientific Quarterly Journal Geosciences* 108:105-114 (In Persian).

Taghizadeh S., Mousivand F., Ghasemi H. (2012) Zakeri Mn deposit, an example of exhalative mineralization in the southwest Sabzevar. *31st PSymposium on Geosciences, Geological Survey of Iran, Tehran, Iran* (in Persian).

Tanaka T., Togashi S., Kamioka H., Amakawa H., Kagami H., Hamamoto T., Yuhara M., Orihashi., Y, Yoneda S., Shimizu H., Kunimaru T., Takahashi K., Yanagi T., Nakano T., Fujimaki H., Shinjo R., Asahara Y., Tanimizu M., Dragusanu C. (2000) JNdi-1: a neodymium isotopic reference in consistency with LaJolla neodymium. *Chemical Geology* 168: 279–281. DOI: https://doi.org/10.1016/S0009-2541(00)00198-4

Tosdal R.M., Munizaga F. (2003*)* Lead sources in Mesozoic and Cenozoic Andean ore deposits, north-central Chile (30–34°S). *Mineralium Deposita* 38: 234-250. DOI: https://doi.org/10.1007/s00126-002-0307-2

Trail D., Watson E.B., Tailby N.D. (2012) Ce and Eu anomalies in zircon as proxies for the oxidation state of magmas. *Geochim, Cosmochim, Acta* 97: 70–87. DOI: https://doi. org/10.1016/j.gca.2012.08.032

Whitney D.L., Evans B.W. (2010) Abbreviations for names of rock-forming minerals. American Mineralogist 95(1): 185–187. DOI: https://doi.org/ 10.2138/am.2010.3371

Wilson N.S., Zentilli M. (2006) Association of pyrobitumen with copper mineralization from the Uchumi and Talcuna districts, central Chile. *International Journal of Coal Geology*, 65(1-2): 158-169. DOI: https://doi.org/10.1016/j.coal.2005.04.012

Wilson N.S., Zentilli M., Spiro B. (2003) A sulfur, carbon, oxygen, and strontium isotope study of the volcanic-hosted El Soldado manto-type copper deposit, Chile: the essential role of bacteria and petroleum. *Economic Geology* 98(1): 163-174. DOI: https://doi.org/10.2113/gsecongeo.98.1.163

Wu J., Kong H., Li H., Algeo T.J., Yonezu K., Liu B., Wu Q., Zhu D., Jiang H. (2021) Multiple metal sources of coupled Cu-Sn deposits: Insights from the Tongshanling polymetallic deposit in the Nanling Range, South China. *Ore Geology Reviews* 139: 104521. DOI: https://doi.org/10.1016/j.oregeorev.2021.104521